Progr Colloid Polym Sci (2001) 118:266–275
© Springer-Verlag 2001

C. Sinn
A. Heymann
A. Stipp
T. Palberg

Solidification kinetics of hard-sphere colloidal suspensions

C. Sinn · A. Heymann · A. Stipp
T. Palberg
Institut für Physik der Johannes-Gutenberg-Universitat, Staudingerweg 7
55099 Mainz, Germany

C. Sinn (✉)
PMS Optik AE/PT, Kölner Strazze 42
60327 Frankfurt, Germany
e-mail: christian.sinn@pms-optik.de
Tel.: +49-65-75001619
Fax: +49-69-75001617

Abstract We investigate the solidification dynamics of hard-sphere colloidal suspensions applying simultaneously small-angle and Bragg light scattering. These experiments allow a consistent picture of nucleation and crystal growth on the level of large-scale density fluctuations and of density fluctuations on the level of individual crystallites. We observe a temporally almost constant nucleation rate after an induction time that decreases with supersaturation. The classical expectation for the nucleation rate density as a function of supersaturation is in accordance with our data. We investigate the validity of the Wilson–Frenkel growth law for hard-sphere systems, which also fits our data satisfactorily. The kinetic prefactors are found to be only 2 orders of magnitude smaller (for nucleation) and 1 order of magnitude larger (for crystal growth) than expected from classical considerations. We discuss the influences of particle size polydispersity on our data.

Key words Colloidal suspensions · Hard spheres · Nucleation and growth · Crystallization kinetics

Introduction

Colloidal suspensions of particles with different pair-interaction potentials have attracted considerable attention because of their possibly generic value. As the particle interaction potential can be tuned experimentally, very different aspects of condensed matter behaviour may be studied on convenient spatial and temporal scales [1]. From a theoretical point of view, a hard-sphere system [2] is beneficial as temperature is not a relevant parameter. The particle concentration (the volume fraction, ϕ) fully determines the equation of state, $\phi Z(\phi) \propto \Pi(\phi)/k_B T$, where Π is the (osmotic) pressure of the system. The equation of state is known in detail over the whole concentration range [3–8]. Experimentally, a hard-sphere suspension has been realized by grafting short polymer hairs on a polymer [9] or silica [10] core and suspending the colloidal particles in a good solvent for the polymer hairs. The van der Waals attraction is reduced by optically matching particles and solvent.

Above the freezing volume fraction $\phi_F = 0.494$, a hard-sphere suspension exhibits coexistence between a fluid and a crystalline phase. Upon increasing the particle volume fraction of the shear-molten fluid, ϕ_{fl}, the crystalline fraction of the sample, X, increase linearly up to the melting point, $\phi_M = 0.545$; $(\phi_{fl} - \phi_F)/(\phi_M - \phi_F)$ is the supersaturation of the system. With higher particle content, the crystalline phase is compressed beyond ϕ_M. The crystalline structure is observed to be face-centred cubic with a considerable amount of stacking faults present. The degree of randomness, however, is not consistent up to now [11, 12].

Whereas the (osmotic) pressure in the coexisting phases can be assumed to be equal at every instant of time [$\phi_{cr} Z(\phi_{cr}) = \phi_{fl} Z(\phi_{fl})$, where ϕ_{cr} is the (metastable) crystal density], the equilibrium of chemical potential ($\mu_{cr} = \mu_{fl}$) is only established within a finite period of time, which can be rather long (about 1 h) for the comparably slow colloidal dynamics. In this period,

crystal nuclei form and subsequently grow. Several investigations have taken advantage of this behaviour in order to determine the crystallization kinetics and, in particular, the temporal evolution of crystal nucleation and growth [13–17]. The results have been interpreted in terms of the classical nucleation theory, an approach first suggested by Russel [18]. A review has been given by one of us of the results obtained with purely repulsive systems recently [19].

In the present work, we demonstrate experiments where we simultaneously perform small-angle and Bragg light scattering. We obtain data sets for the temporal evolution of the number of crystals and their size, and these are consistent on the level of the individual crystallites and on the level of long-range density fluctuations as well. We determine the nucleation rate densities at different supersaturations and compare them with classical nucleation theory. We also report crystal growth data in view of the Wilson–Frenkel growth scenario. Our data allow a numerical comparison with results from atomic and molecular systems. In addition, we assess the influence that polydispersity has on our data.

Classical crystallization theory

Nucleation kinetics

The classical picture of nucleation assumes a statistical particle density fluctuation in the metastable melt that forms an ordered cluster in the surrounding fluid [20, 21]. Whether this initial cluster is stable (and grows) or unstable (and disappears) is governed by competition between the surface energy of the cluster, given by the (macroscopic) fluid–crystal surface tension, γ, and the gain of energy upon crystallization. The radius of the critical cluster, R_c, can be calculated by minimizing the free energy. Following Kelton [22], the molar nucleation rate, j, can be written as

$$j = 8\left(\frac{6}{\pi}\right)^{1/3} \frac{DN_L \bar{V}^{1/3}}{\xi^2} \left(\frac{\gamma}{k_B T}\right)^{1/2} \exp\left(-\frac{16\pi\gamma^3 \bar{V}^2}{3k_B T(\Delta\mu)^2}\right) , \quad (1)$$

where D is the diffusion coefficient of the particles and ξ is the mean path length for the diffusion of the particle to the cluster surface. N_L is Avogadro's number and $\bar{V}$ is the average volume per molecule. $\Delta\mu$ is the chemical potential difference between the initial phase and the nucleated phase and $k_B T$ is the thermal energy. Equation (1) has been used in a recent numerical study of nucleation and growth in methanol [23]. This allows a detailed comparison between the behaviour of molecular and colloidal matter. For hard-sphere colloidal crystals, the nucleation rate density, J, is the appropriate quantity that is experimentally accessible [18, 24]. We modify Eq. (1) correspondingly. For the mean path length of diffusion, we adopt the mean interparticle distance in the metastable fluid, $\xi = 2r/\phi_{fl}^{1/3}$, with r the radius of the colloidal particles. The average volume per particle in the growing nucleus can also be expressed in terms of the cluster particle volume fraction, ϕ_{cl}, $\bar{V} = 4\pi r^3/3\phi_{cl}$. This gives

$$J = K_N \frac{D\phi_{fl}^{5/3}}{r^5} \exp\left(-\frac{4\pi^3\gamma^{*3}}{27\phi_{cl}^2(\Delta\mu^*)^2}\right) , \quad (2)$$

where $K_N = 6\gamma^{*1/2}/\pi\phi_{cl}^{1/3}$, $\Delta\mu^* = \Delta\mu/k_B T$ and $\gamma^* = 4r^2\gamma/k_B T$. From the equation of state, the density of the crystals, ϕ_{cr}, as well as the chemical potential difference, $\Delta\mu^*$, can be calculated as a function of the density of the metastable fluid. Transient compression effects are not included since we set $\phi_{cl} = \phi_{cr}$. For the fluid phase, we use the equation given by Carnahan and Starling [4], whereas for the crystalline phase we use that given by Young and Alder [6]. The combination of both equations, yielding the equilibrium properties, can be solved only numerically. We therefore approximate the exact results with an error of less than 1% by the following quadratic forms [25]:

$$\phi_{cr}(\phi_{fl}) = 0.5455 + 1.308(\phi_{fl} - \phi_F) - 2.93(\phi_{fl} - \phi_F)^2 \quad (3)$$

$$\Delta\mu^*(\phi_{fl}) = -10.354(\phi_{fl} - \phi_F) - 56.23(\phi_{fl} - \phi_F)^2 \quad (4)$$

These equations are used together with Eq. (2) for the data evaluation. $\phi_{cr}^{1/3}$ exhibits no significant variation as a function of ϕ_{fl}. Accordingly, we regard K_N as constant in the evaluation process. Besides K_N, the only parameter that governs the nucleation rate in hard-sphere colloidal systems is expected to be the crystal–fluid surface tension, γ^*, which we regard here as a fitting parameter. Theoretical studies predict either $\gamma^* \approx 0.3$ [26, 27] or $\gamma^* \approx 0.6$ [28–30]. Experimental results [13, 31] seem to indicate that the appropriate value may be close to $\gamma^* \approx 0.55$.

Wilson–Frenkel growth

For the quantitative description of the growth kinetics of a cluster that exceeds the critical radius, we use the growth law proposed by Wilson and Frenkel [21]

$$v = v_0[1 - \exp(\Delta\mu^*)] , \quad (5)$$

which has been successfully used already to describe the crystal growth process in charged colloidal samples [32, 33]. The user of Eq. (5) implies the following restrictions with regard to the growth process. First, the growth is assumed to be linear in time, that is, we have interface- (or reaction-) limited growth. Accordingly, the maximum growth velocity is determined by the incorporation of the

particles into the crystal surface. In contrast, diffusion-limited growth predicts a growth law proportional to the square root of time. This would slow the crystal growth in the coexistence region because of the density difference between the liquid and the crystal, which is absent above ϕ_M. We shall come back to this point later. Furthermore, we assume normal growth for the crystal growth process, meaning that the growth kinetics is independent of the surface site. This necessarily implies a rough surface, leading to nonfaceted crystallites. This is in line with observations of He et al. [34], who found rough surfaces of hard-sphere crystals with the aid of light microscopy; however, they also observed growth instabilities that lead to anisotropic, nonspherical crystals. A dendritic growth process has been observed under conditions of microgravity [35].

The factor v_0 can be interpreted as a typical velocity for particles to be incorporated into the crystal surface, while the second term is the probability for them to be incorporated into the growing crystal. As colloidal particle dynamics is overdamped, we assume v_0 to be governed by the diffusion of the particles over a certain distance, $v_0 = D/\xi$. As before, we take the mean interparticle distance in the metastable fluid, $\xi = 2r/\phi_{fl}^{1/3}$.[1]

In order to describe the experimental data within the framework of the theory, one has to decide which diffusion coefficient to use. Whereas it seems to be evident that incorporation particle dynamics has to be described by self-diffusion, it is not immediately clear whether to regard the self-diffusion in the limit of short or long times. This question has been discussed in detail by van Duijneveldt [24], who suggested using a diffusion coefficient that is affected by the nearest-neighbour cage, because ξ is of the order of the dimension of the particles. In addition, he suggested using the long-time self-diffusion coefficient, because it seemed to be consistent with the experimental data. We follow his argumentation and choose the long-time self-diffusion coefficient,

$$D_s^* = \frac{D_s^L(\phi_{fl})}{D_0} = \left(1 - \frac{\phi_{fl}}{0.58}\right)^{\delta} , \qquad (6)$$

normalised by $D_0 = k_B T/(6\pi\eta r)$, the Stokes–Einstein diffusion coefficient of an isolated colloidal particle in a medium of viscosity η. Van Duijneveldt used $\delta = 1.76$, whereas the theoretical prediction of Tokuyama and Oppenheim [36] yields $\delta = 2$ at high volume fractions. Our choice of $\delta = 2.58$ provides the advantage that Eq. (6) has been obtained experimentally with hard-sphere colloidal suspensions very similar to ours at volume fractions close to the glass transition. Hence, our growth law reads

$$v = K_G \frac{D_s^* \phi_{fl}^{1/3}}{r} [1 - \exp(\Delta\mu^*)] \text{ with } K_G = \frac{1}{2} . \qquad (7)$$

As before, the chemical potential difference is completely determined by the equation of state in the form of Eqs. (3) and (4), which means that only one fitting parameter (K_G) remains.

[1] In Ref. [19], a slightly different definition of ξ was used, and this leads to numerically different values for the kinetic prefactors

Experimental

Light scattering apparatus

The light scattering apparatus was constructed specifically for our approach [25]. A scheme of the setup can be found elsewhere [19]. The vertically polarized beam of He–Ne laser (632.8 nm) is spatially filtered by a combination of a microscope objective (10x), a pinhole (diameter: 40 μm) and an asymmetric biconvex lens ($f' = 100$ mm). The distance between the pinhole and the biconvex lens is adjusted such that the transmitted beam is not collimated, but is focused onto the beam stop of the small-angle detector, located at a distance of about 150 cm. The cuvette with the colloidal suspension under study is located in a sample cell filled with a decahydronaphthalene (DHN) 1, 2, 3, 4-tetrahydronaphthalene (THN) mixture. The light beam enters the sample cell through a glass window. The Bragg scattered light leaves the sample cell through a spherical lens, which consists of a sector of a sphere (radius 50 mm, thickness 40 mm). The vortex of the lens was ground to form a plane exit window perpendicular to the optical axis of 12.5-mm diameter. The entrance window and the spherical lens are made from K10 (Schott), which has a refractive index close to the suspending fluid (see later). The centre of the cuvette is located at the front focal point of the spherical refracting surface. This optical setup guarantees that light scattered under equal angles in the illuminated volume is collected in a single point on the back focal plane of the spherical surface, where the Bragg detectors are located. On the Bragg detector post, six photodiode detector units are arranged concentrically around the spherical lens at a distance of 10 cm. Three units are arranged linearly on the small-angle detector post. Both posts are mounted onto a large aluminum frame, which is rotated about the optical axis by a stepper motor that performs a full rotation with 6272 steps. In this way, the complete two-dimensional scattering pattern is accessible. After each step (approximately 0.06°), the scattered intensity measured by the photodiodes is digitized and stored for further evaluation by a personal computer. A single measurement takes about 40 s. In order to enhance the statistical accuracy of the results, we angularly average in this contribution the intensities for every individual q. Angularly resolved measurements have been applied earlier to study heterogeneous nucleation at the cuvette walls [37]. We note that polarization effects in the Debye–Scherrer rings are superimposed by multiply scattered light. Corrections for multiple scattering were generally found to be unnecessary in the q region investigated here [25]. We calibrated the apparatus using an optical grid that was immersed into the index-matching bath. The accessible Bragg scattering vector range ($n = 1.5$) is $q = 5.5$–$18.9\,\mu m^{-1}$ with a resolution of $\delta q = 0.15\,\mu m^{-1}$. This comparatively large angular range allows the time evolution of different Bragg peaks to be measured. For small-angle scattering the range is $q = 0.02$–$0.81\,\mu m^{-1}$ with a resolution of $\delta q = 0.012\,\mu m^{-1}$.

Before starting a series of individual measurements, the colloidal suspensions were shear-molten by a slow rotation of the cuvette for several hours or days. This should destroy any crystalline order within the suspension. Stopping the rotation and inserting the cuvette into the sample cell defines $t = 0$ for the measurement series. The sample cell is thermostatted with Peltier

elements to better than 0.1 K. This stability is necessary in order to maintain the refractive index matching in the course of the measurements.

Sample preparation

The particles used comprised a poly(methyl methacrylate) (PMMA) core with short hairs of poly(hydroxy stearic acid) (PHSA) grafted onto the surface. They were synthesized by Underwood (SMU28, [38]) and have been carefully characterized for their radius and the corresponding size polydispersity by static light scattering [39]. We obtained a particle core radius of $r = (435 \pm 4)$ nm and a remarkably low size polydispersity of 2.5%. The effective hard-sphere radius of these particles ($r = 445$ nm, determined from the phase boundaries) is consistent with the expectation of a hairy layer of approximately 10 nm [3].

The particles were suspended in a suitably chosen mixture of DHN (isomeric mixture) and THN (both from Merck, Germany). The mixing ratio was adjusted such that the solvent matches the refractive index of the particles. A complete match of the refractive indices of particle and solvent is virtually impossible for a core–shell system. We therefore adopted the following empirical procedure. The particles were suspended in pure DHN to yield a high volume fraction. A strongly turbid sample resulted. We added THN and observed a strong decrease in turbidity. Close to the optimal index matching point of approximately 35% THN by volume, the turbidity does not change significantly. Alternatively, we observed the dispersive behaviour of the sample. A slight surplus of THN at the matching point leads to bluish appearance of the sample when observed under white light illumination, whereas a surplus of DHN leads to a yellowish appearance. We always tried to obtain a purple transmission, indicating the matching point.

The immediate requirement for performing crystallization measurements of hard-sphere suspensions is a sample of exactly known particle volume fraction. Owing to a limited amount of colloidal material, we adopted the following procedure for fixing ϕ. We prepared a diluted suspension by adding DHN and THN to a colloidal sample until index-matching was achieved. The suspensions as well as the solvents were filtered using 5-μm polytetrafluoroethylene filters; the complete procedure was performed in a laminar flow box. The suspension was filled into a rectangular cuvette (10 × 5 × 20-mm inner volume). The particles were centrifuged to form a compact sediment of $\phi \approx 0.64$, and a sufficient amount of supernatant liquid was removed to obtain a concentrated sample ($\phi \approx 0.57$) for the first light scattering measurement. Subsequently, we diluted the sample with the supernatant liquid removed before, the amount of solvent added being controlled by weight, and investigated this diluted sample. We terminated the series at a volume fraction where nucleation becomes very slow. We then determined the effective hard-sphere volume fraction of the last sample using the sedimentation method described Paulin and Ackerson [40], where the sample volume fraction is obtained from an extrapolation of the respective volumes of the liquid and the solid phase to $t = 0$. We note that the uncertainty of this determination is mainly given by the theoretical values for ϕ_F and ϕ_M. The concentration of every sample investigated in our dilution series was calculated using $\rho_{PMMA} = 1.188\,g/cm^3$, a value close to that used by Phan et al. [3].

In this investigation, we report results for two different dilution sequences. The difference in the hard-sphere volume fractions observed during these runs stems from the slight evaporation of the solvent despite careful sealing.

We finish this section by noting that THN, over periods of several weeks, slowly penetrates the particle core [3, 39]. This has already been observed for a different solvent [41]. This observation prohibited us from using calculated particle form factors for data correction purposes. We therefore used the scattering of the shear-molten state as a reference and note that in the course of a single solidification measurement the refractive index variation within the particles remains constant.

Data evaluation and experimental results

Small-angle scattering

Small-angle light scattering experiments are plagued by parasitic light scattering from dust or optical inhomogenities from the optical surfaces. As described before, we kept the number of transmitted surfaces low. Nevertheless, we observed strong background scattering. In order to correct for this background, we subtracted an early measurement from our data. We observed a clear-cut peak at finite q, which grew with time and became narrower. The maximum intensity shifted towards smaller q.

The observation of a peak in the small-angle scattering intensity, though in accordance with different studies [13, 15, 24], still lacks a quantitative explanation. Qualitatively, the peak results from large-scale variations of the refractive index with overall conservation of the particle number density or the mean refractive index; thus, $i(q \to 0) = 0$. Its shape is determined from details of the density fluctuations and their spatial distribution. In crystallization, it may stem from the crystal and the surrounding depletion zone, which, however, may change in the course of time [42]. In the present contribution, we focus on the temporal evolution of the peak and leave a structural explanation for further investigations.

With progressing solidification, the maximum peak intensity, $i_{max} \propto NR^6$, increases, because either the number of crystals in the scattering volume increases or the individual crystals grow. Both processes result in a shift of the peak towards smaller q values. A strong aid in the data evaluation is the observed scaling of the small-angle scattering peak [13] according to

$$i(q,t) = i_{max}(t) F[q/q_{max}(t)] \quad , \tag{8}$$

where $F(Q)$ is a universal model function for $Q = q/q_{max}(t)$. Several functional forms for $F(Q)$ have been suggested in the literature [13, 15]. For the present evaluation, we modify the standard Furukawa function [43], which harmonically adds a low-q Q^2 dependence to a large-q $Q^{-\delta}$ dependence. We add a constant, C, that is independent of Q and obtain

$$F(Q) = \frac{\delta + 2 + C}{\delta Q^{-2} + 2Q^{\delta} + C} \quad . \tag{9}$$

For spinodal decomposition, $d = \delta - 1$ is the fractal dimension of the surfaces, which is frequently found to be $d = 3$. As we have no a priori information about the structure of the depletion zones, we regard δ as a free parameter. The combination of Eqs. (8) and (9) yields

$$i(q)/i_1 = \left[1 + \left(\frac{q}{q_1}\right)^{-2} + \left(\frac{q}{q_2}\right)^{\delta}\right]^{-1} \quad , \tag{10}$$

with the fitting parameters $i_1 = i_{max}(\delta + 2 + C)$, $q_1 = q_{max}(\delta/C)^{1/2}$ and $q_2 = q_{max}(C/2)^{1/\delta}$.

With great caution, $1/q_1$ may be interpreted as the characteristic extension of the crystal, and $1/q_2$ as the extension of the depletion zone. However, providing a structural model is beyond the scope of this contribution and requires data of still improved statistical quality; therefore, we used Eq. (10) as a fitting function only and obtained from this fit i_{max} and q_{max}, from which $N(t)$ and $R(t)$ can be calculated [25]. For technical reasons, we determined $q_{1/2}$ instead of q_{max}, which is defined as the larger q value of $F(Q_{1/2}) = 1/2$ and can be evaluated very similarly to q_{max} [13]. The results are collected in Fig. 1. We shall return to a detailed discussion of the data in a subsequent section.

Bragg scattering

Owing to the close match of the refractive indices, we assume that the scattered light intensity can be calculated using the Rayleigh–Debye–Gans approximation. Accordingly, we write the scattered intensity in the Bragg range as a product of the individual particle form factor, $P(q)$, and different structural contributions

$$I(q,t) \propto P(q)\left[S_{\mathrm{Bragg}}(q,t) + S_{\mathrm{diff}}(q,t) + S_{\mathrm{fluid}}(q,t)\right] \ , \tag{11}$$

where S_{fluid} is the structure factor of the fluid phase, S_{Bragg} describes the Bragg reflections of the crystals, and S_{diff} gathers contributions from grain boundaries or crystal imperfections. The respective weights of the different structures vary with time as solidification proceeds; S_{Bragg} and S_{diff} may also alter their q variation. For S_{Bragg}, this originates, for instance, from the relaxation of the initial compression of the crystals. S_{diff} on the other hand, may reflect the increasing number of crystalline imperfections in larger crystals. S_{fluid} comprises contributions of the fluid structure factor of the metastable fluid and of the structure factor of the equilibrium fluid. The latter contribution is absent for $\phi_{\mathrm{fl}} > \phi_{\mathrm{M}}$; the q dependence of the former could be calculated using the Percus–Yevick structure factor for ϕ_{fl} [44].

As discussed earlier, the particle form factor is not available with sufficient accuracy. Accordingly, we divide our data by an early measurement

$$i(q,t) = \frac{I(q,t)}{I(q,0)} = \frac{S_{\mathrm{Bragg}}(q,t)}{S_{\mathrm{fluid}}(q,0)} + B(q,t) \ , \tag{12}$$

where $B(q,t)$ is a baseline which is allowed to change only slowly and continuously as well as with time as with q. In addition, we require that the fluid structure does not lead to considerable distortions of the individual Bragg reflection. It is then possible to isolate the reflection's time dependence for further quantitative analysis.

The requirements as mentioned earlier are well established for the (2 2 0) and the (3 1 1) peaks only. As discussed in detail earlier [37], we observed that the (3 1 1) peak is influenced for our particles by scattering contributions from oriented close-packed planes that exhibit different growth kinetics. We therefore restrict ourselves here to the temporal evolution of the (2 2 0) lattice peak and note that the evolution of (3 1 1) and (1 1 1) could be determined without disturbing side effects using particles with a different size.

Because the crystalline samples under investigation consist of randomly oriented crystals, the Bragg structure factor we measure appears in the shape of Debye–Scherrer rings centred about the optical axis of the experiment. The structure factor is therefore an average over different crystallite orientations. In addition, the individual crystals are not large compared to the wavelength, meaning that the crystal form factor has to be taken into account, which leads to a finite width, Δq, of the Debye–Scherrer ring. The angular averaged intensity of the Debye–Scherrer ring is accordingly given by

$$S_{\mathrm{Bragg}}(\Delta q,t) = \iint_{q=G+\Delta q} S_{\mathrm{Bragg}}(|\vec{q} - \vec{G}|,t)\mathrm{d}^2 q \ , \tag{13}$$

where $\vec{G}$ is the reciprocal lattice vector. We assume that the scattering of a spherical crystal of radius R can be described by a Rayleigh–Debye–Gans form factor, centred at $\vec{q} = \vec{G}$. We evaluate Eq. (13) in the limit of $\Delta q << q$ and obtain

$$S_{\mathrm{Bragg}}(\Delta q,t) \propto \left[1 - \cos(2\Delta qR) - 2\Delta qR\sin(2\Delta qR) + 2\Delta q^2R^2\right]/(2\Delta q^4R^4) \ . \tag{14}$$

Hence, $S_{\mathrm{Bragg}}(\Delta q,t)$ given by Eq. (14) is the shape factor of the individual crystallites, averaged in reciprocal space over every crystal orientation. In turn, the use of Eq. (14) allows us to extract the typical dimensions, R, of the crystallites from the width of the Bragg peak that we obtain by angular averaging over the Debye–Scherrer ring.

The scattered intensity is proportional to the shape factor times the crystalline volume squared times the number of crystals N times an optical constant representing the scattering strength. For the scattered intensity integrated over the Bragg peak, we thus obtain

$$i_{\mathrm{peak}}(t) = I_0 \int_{q_1}^{q_2} N(t)R(t)^6 S_{\mathrm{Bragg}}(\Delta q,t)\mathrm{d}\Delta q \propto N(t)R(t)^3 \propto X(t) \ , \tag{15}$$

where the integration is restricted to those q values where the Bragg peak differs from the baseline. $X(t)$ is the crystalline fraction of the sample. The results for $N(t)$ and $R(t)$ are shown in Fig. 2, which can be compared directly with the small-angle scattering data shown in Fig. 1.

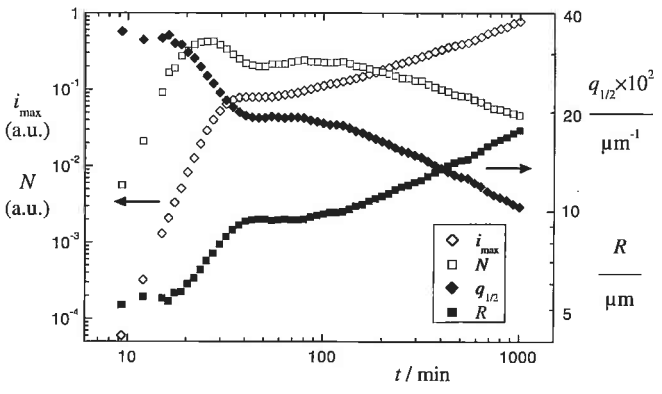

Fig. 1 Temporal behaviour of the maximum intensity, $i_{\max}$, the characteristic scattering vector, $q_{1/2}$, the crystal number density, N, and the average crystal size, R, calculated from the small-angle scattering data. The sample volume fraction is $\phi_{\mathrm{fl}} = 0.538$

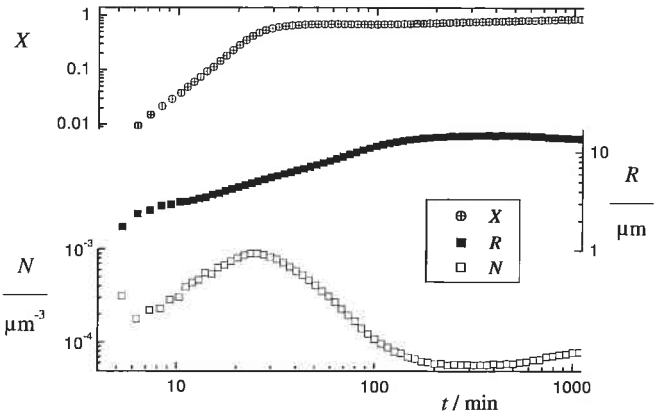

Fig. 2 Temporal behaviour of the crystalline fraction, X, R and N calculated from the Bragg scattering data. The sample volume fraction is $\phi_{\mathrm{fl}} = 0.538$

Merging of the small-angle and Bragg scattering data

We have shown that $N(t)$ and $R(t)$ can be obtained from small-angle and Bragg scattering data independently. The data very satisfactorily exhibit the same qualitative and quantitative behaviour [25, 45]. This redundancy can be used to obtain a set of $N(t)$ and $R(t)$ of improved statistical quality upon merging these data. In addition, some experimental limitations of both individual methods can be removed from the data.

First, we observed that $R(t)$ never exceeded $R = 15\,\mu$m in the Bragg data, though the corresponding width of the Bragg peak is larger than the experimental resolution. No individual experimental uncertainty (such as the converging incident light beam, lens aberrations or an incorrect lens adjustment) can explain this broad reflection; however, a combination of these effects may play a role. The small-angle scattering data, on the other hand, are readily prone to saturation effects of the photodiodes, as the scattered light intensity as a function of time and of sample concentration varies over orders of magnitude. Whereas the data at large ϕ exhibit a low signal-to- noise ratio, the scattered light of the samples at small ϕ saturates the detector.

We therefore proceeded as follows. First, we compared the crystal radii, $R(t)$, as obtained from both methods and decided on the most reliable values on the basis of the standard deviation of the respective fit and the saturation limits mentioned. The results are shown in Fig. 4. The use of the model functions as described previously leads to a systematic deviation between the small-angle and the Bragg data, which can be removed by dividing the small-angle data by 1.19 [19]. The reason for this deviation for $t \to \infty$ stems from the different structural origin of the small-angle and the Bragg data: only the latter yield the radius of the crystals immediately, whereas for the former the radius is less well defined (see the discussion earlier). Next, we determined the crystalline fraction, $X(t)$, from the Bragg scattering data by normalisation of $i_{\text{peak}}(t)$ by its long-time limit, $i_{\text{peak}}(t \to \infty)$. For samples below ϕ_M, the expected crystalline fraction is taken into account.[2] Assuming that $X(t)$ is identical for the small-angle and the Bragg scattering data, we normalized the small-angle scattering data correspondingly. Again, we selected the most reliable data. From $X(t)$, we calculated $N(t)$; the results are shown in Fig. 3. From the initial slope of these data, we obtained the nucleation rate density, $J = \mathrm{d}N/\mathrm{d}t$, and the growth rate, $v = \mathrm{d}R/\mathrm{d}t$.

Comparison of theory and experiment

The results for the temporal evolution of the number of crystals are shown in Fig. 3. As a general observation, we find a roughly linear increase of $N(t)$, followed by a saturation or even a decreasing number of crystals. We interpret this behaviour as the transition from a nucleation and growth period to ripening behaviour, where the larger crystals grow at the expense of the smaller ones, and we restrict our evaluation to the former process. In addition, the nucleation seems to start with a delay for most of the samples. The data for the temporal evolution of the crystal radii, which are shown in Fig. 4, also exhibit this induction time, together with a finite minimum crystal size. Subsequently, the data points show a more-or-less linear increase of the crystal size.

Induction time

Subsequent to the induction time, t_I, the nucleation rate is found to be almost constant. Only a double-logarithmic plot of $N(t)$ exhibits noticeable, but small, deviations from linear behaviour. Harland and Van Megen [17] observed different behaviour for similar data sets. Their number densities of crystals exhibited a temporal power-law behaviour with exponents up to 3, a behaviour they termed accelerated nucleation. A comparable behaviour is absent in our data. We therefore prefer to speak about a delayed nucleation, which gives rise to small nonlinearities in a double-logarithmic plot. From Fig. 3, we obtain t_I by a linear extrapolation of $N(t)$, that is, $N(t_I) = 0$. The corresponding data are collected in Fig. 5. The induction time is found to decrease with increasing supersaturation, saturating at approximately ϕ_M with $t_I = 4$ min. The minimal cluster radius exhibits a similar behaviour, the saturation value being approximately 2 μm, equivalent to 1–2 lattice constants or 2–3 particle diameters.

These results agree very well with the classical picture of nucleation. The nucleation rate is assumed to be constant up to that time where ripening sets in, in accordance with our data. In addition, the initial nonlinear behaviour (the induction time) can be well understood, as the system needs some time to acquire a steady-state cluster distribution after the fast quenching into the coexistence region [22]. This period of time should decrease with increasing supersaturation, because the critical radius decreases drastically, in agreement with our data and those reported by Harland and van Megen [17]. Upon approach of the glass transition, the decreasing diffusion coefficient may lead to an again increasing induction time, as clearly visible in the data of Harland and van Megen; however, our data do not reproduce this trend [19].

Nucleation and growth rates

In proceeding further, we determined the normalized nucleation rate density, J^*, as a function of supersaturation from the data shown in Fig. 3. Where the slope changes slightly, we used the initial slope only. As shown before, classical nucleation theory predicts

$$J^*(\phi_{fl}) = \frac{Jr^5}{K_N D_0} = D_s^*(\phi_{fl})\phi_{fl}^{5/3} \exp\left(-\frac{4\pi^3\gamma^{*3}}{27\phi_{cr}^2(\phi_{fl})(\Delta\mu^*(\phi_{fl}))^2}\right), \quad (16)$$

[2] This procedure has been cross-checked by the observation that $i$peak$(t \to \infty)$ is constant above ϕ_M to within a systematic error 20%. If we calculate, using this value, $X(t)$ for samples below ϕ_M, we obtain the values that are predicted by the phase diagram. Interestingly, Harland and coworkers [16, 17] report $X(t \to \infty) \neq 1$ above ϕ_M, as yet unexplained

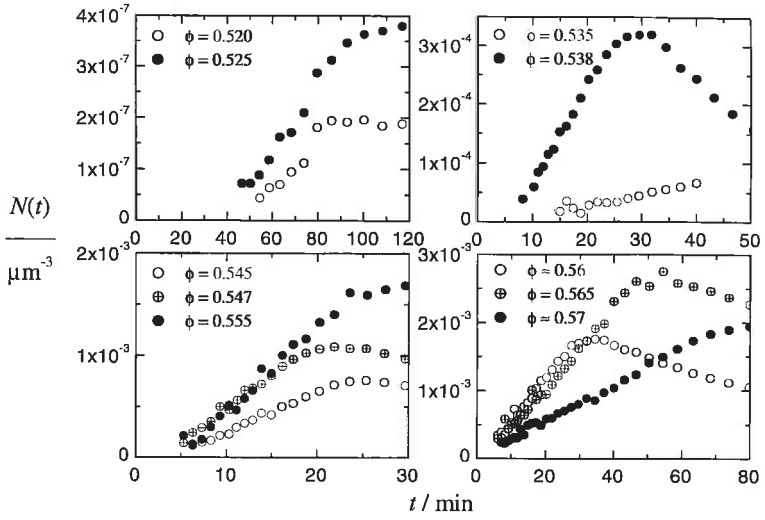

Fig. 3 Temporal behaviour of the crystal number density, $N(t)$, for selected samples with the volume fraction indicated. Notice the scale variation

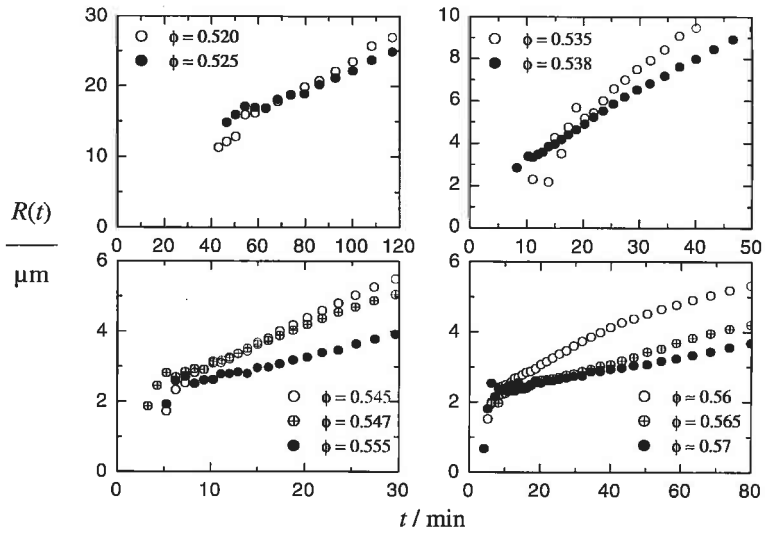

Fig. 4 Temporal behaviour of the average crystal sizes, $R(t)$, for selected samples with the volume fraction indicated. Notice the scale variation

where we are left with only two adjustable parameters, that is, the surface tension γ^* and K_N. The diffusion coefficient is specified by Eq. (6) and $\phi_{cr}(\phi_{fl})$ and $\Delta\mu^*(\phi_{fl})$ by Eqs. (3) and (4). The corresponding data together with a fit of Eq. (16) are shown in Fig. 6. The expected functional dependence of $J^*(\phi_{fl})$ is in excellent agreement with our experimental data. The surface tension we determine from this fit is $\gamma^* = 0.51$, close the theoretical expectation for hard-sphere crystals reported by Marr and Gast [31] and almost identical to the value read from the data of Harland and van Megen [17]. The kinetic prefactor amounts to $K_N = 0.013$, which is remarkably close to the value used by Harland and van Megen to fit their data ($K_N = 0.01$). We keep a discussion of K_N for the end of this section. Similarly, we determined the normalized growth velocity, v^*,

$$v^*(\phi_{fl}) = \frac{vr}{K_G D_o} = D_s^*(\phi_{fl})\phi_{fl}^{1/3}[1 - \exp(\Delta\mu^*(\phi_{fl}))] \qquad (17)$$

from the data shown in Fig. 4. We determined an initial linear slope from $R(t)$ and regard the radius offset as the crystal radius R_c, corresponding to the induction time t_I. The data obtained are shown in Fig. 7 together with a fit to the theory. Again, the agreement between theory and experiment is very good. The kinetic prefactor $K_G = 15$ is the only adjustable parameter.

The data at small volume fractions seem to deviate increasingly. This may have two different reasons. On the one hand, the diffusion coefficient we choose may become inadequate. This would not be noticed in the nucleation data, as these are dominated by the increase in the surface contribution at low ϕ_{fl}. We recall from the previous discussion that the choice of the functional form

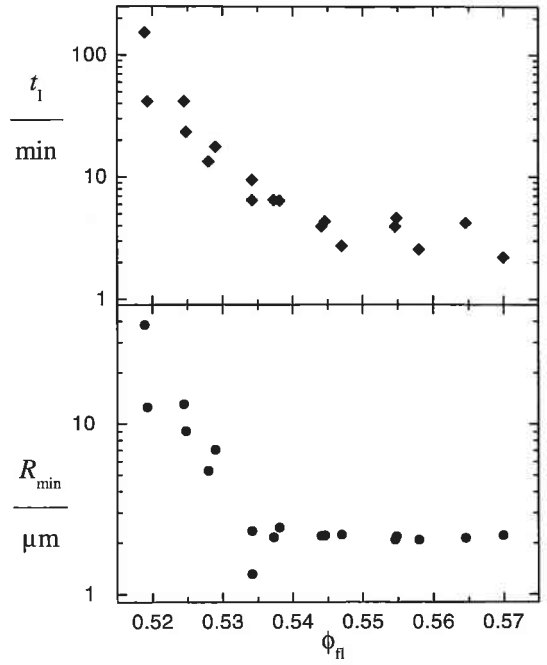

Fig. 5 Induction time, t_l, and minimal crystal size, R_{min}, as a function

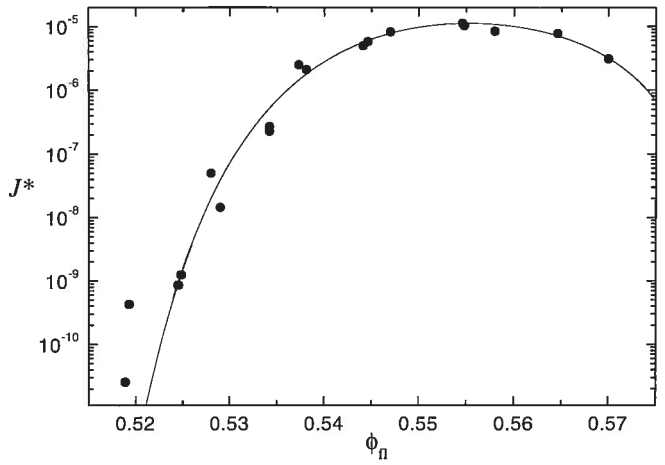

Fig. 6 Nucleation rate, J^*, as a function of the sample density, ϕ_{fl}. The *solid line* is a calculation according to the classical nucleation theory. The fitting parameters are the surface tension $\gamma^* = 0.51$ and the kinetic prefactor, $K_N = 0.013$

for the self-diffusion coefficient is not unequivocal. In addition, at smaller volume fractions even collective diffusion may come into play owing to the increasing density differences between the metastable fluid and the crystal phase.

On the other hand, the growth velocities were obtained assuming $R(t) \propto t$. One might argue that a diffusion-limited growth process with $R(t) \propto t^{1/2}$ would better describe our data. This would, however, be

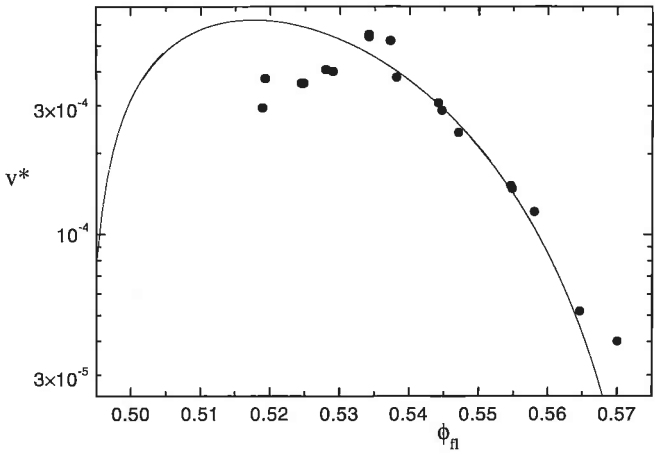

Fig. 7 Growth velocity, v^*, as a function of ϕ_{fl}. The *solid line* is a calculation according to the Wilson–Frenkel growth law. The single fitting parameter is the kinetic prefactor, $K_G = 15$

difficult to observe, because at high volume fractions the crystallization is fast and $R(t)$ is dominated by ripening. In addition, at early times the limited number of data will probably always yield a linear relationship. The growth exponents we determine lie between the extreme cases of 0.5 and 1. Diffusion-limited growth should have the most pronounced influence on the data where the crystallization is slow, that is, at low ϕ_{fl}, where we observe the data deviate.

Kinetic prefactors

Besides the results presented so far, the kinetic prefactors deserve further attention, because they appear to span orders of magnitude in experimental investigations of atomic and molecular system [22].

If we use the appropriate length scales for colloidal systems, we expect $K_N \approx 1.6$ for $\gamma^{\infty} = 0.51$ and $\phi_{cr} = 0.6$ (cf. Eq. 2). The experimentally determined value is approximately $K_N = 0.013$, which is 2 orders of magnitude smaller than the theoretical value. The opposite is true for K_G, where the experimentally determined value of 15 is 1 order of magnitude larger than the predicted value of 0.5.

It should now be possible to compare these results with those reported for atomic or molecular systems. Unfortunately, these data exhibit an inconsistent picture [22]. Whereas, for instance, K_N for liquid Hg is reported to be 7 orders of magnitude higher than expected, the kinetic prefactors for different *n*-alkanes seem to be in accordance with expectation, and the nucleation rate as a function of supersaturation is in accordance with the classical theory. The deviation for liquid Hg can be explained if the surface tension is modelled as temperature-dependent. Gránásy Iglói [46] drew a similar con-

clusion. They compared different nonclassical nucleation theories, divided into modifications of the classical theory and density functional approaches. From a comparison with experimental data, they concluded that a modification of the surface energy assuming a diffuse interface correctly predicts the experimentally determined nucleation rates, whereas density functional approaches fail to provide agreement with experimental data.

In a recent study, Brugmans and Vos [23] investigated the nucleation and crystal growth in methanol subjected to high pressures. In their study, supersaturation was proportional to a pressure difference. They found excellent agreement of their nucleation rate data with the classical theory and of their growth rate data with the Wilson–Frenkel law. In the latter case, even K_G could be reproduced with reasonable assumptions, whereas K_N was found to be 20 orders of magnitude lower than expected, with no explanation given.

In view of these partly contradictory results for atomic and molecular systems, the agreement between classical theories and experimental data appears to be remarkably good for hard-sphere colloidal systems. Even the kinetic prefactors differ (only) by 1 or 2 orders of magnitude from expectation. In particular, the simple idea of a sharp interface with a macroscopically defined surface tension between the crystal nuclei and the surrounding fluid seems to be effective. Experimental and theoretical values for the surface tension are in good agreement with each other.

Particle polydispersity

Recently, the influence of the particle size polydispersity on hard-sphere crystallization has been discussed. In view of the results presented here, some comments seen to be appropriate.

Bolhuis and Kofke [47] predicted from Monte Carlo simulations a shift of the phase boundaries that amounts to $\phi_F = 0.502$ and $\phi_M = 0.550$ for a Gaussian-distributed 5% particle size polydispersity. The particle we used in the present study exhibited a remarkably low polydispersity of 2.5%. Accordingly, we expect that the shift of the freezing volume fraction owing to polydispersity should be rather small. As the effective hard-sphere radius, calculated from ϕ_M, is in very good agreement with expectation, we estimate that the phase boundaries we use are not prone to polydispersity effects. Again owing to the small polydispersity of our particles, we also expect no fractionated crystallization as reported by Bartlett [48]. However, the nucleation and growth rates themselves may be influenced by polydispersity. Henderson et al. [49] measured a tenfold reduction of the nucleation rate upon increasing the particle size polydispersity from 6 to 11%. They explain this effect by a (comparably slow) ejection of nonfitting particles from the crystal that is composed of the majority particle fraction; however, with small polydispersities like those of the present study, the fraction of nonfitting particles is very low and will probably influence the growth kinetics only at late stages, where the crystal attains it final composition, while the nucleation rate may not be influenced at all. From the classical theory, we can estimate the polydispersity effect on J by calculating ϕ_{cl}, assuming a cluster of a single particle with 2.5% radius deviation surrounded by four particles having nominal radii. Obviously, a smaller particle increases the nucleation rate, whereas a larger one leads to a decreased nucleation rate. In this model, the average nucleation rate therefore remains unchanged by (a symmetrical) polydispersity. In addition, the numerical effect is very small (approximately 5%) and does not explain the observed discrepancy for K_N.

A different origin for the influence of polydispersity on the crystallization has been observed by Phan et al. [50]. They found significant deviations from the crystalline equation of state with increasing polydispersity and suggested a model crystal structure, where smaller particles tend to surround larger ones, thereby reducing the crystalline packing fraction. Again, the small polydispersity of the particles in the present study prohibits us from noticing any effects related to their observation.

If we bear in mind that the choice of the correct functional form of $D(\phi_{fl})$ has a strong influence on the observed crystallization kinetics, an unequivocal determination of the effect of polydispersity on the kinetic prefactors seems to be very difficult. The important question, however, is, whether the observed deviation of the kinetic prefactors from expectation is a manifestation of a generic trend. Our data seem to favour this interpretation. As critical cluster formation as well as crystal growth are dominated by very similar particle dynamics, we are not aware of any mechanism where polydispersity causes a decrease in the nucleation rate and an increase in the growth rate at the same time.

Conclusion

We have shown that hard-sphere colloidal suspensions exhibit both, qualitatively and quantitatively, the dependence predicted by classical theories for crystal nucleation and growth as a function of supersaturation. The nucleation rate density is found to be 2 orders of magnitude slower, the crystal growth rate is found to be 1 order of magnitude faster compared to theoretical considerations. In view of the results for atomic and molecular systems, however, this deviation is small.

The small numerical deviation may be explained by the combined influence of a wrong estimate for the diffusion coefficient, the length scale involved and the

particle polydispersity. Unfortunately, the results for atomic and molecular systems reported so far exhibit no clear trend to allow a unique comparison. As long as the experimental observations for atomic and molecular systems cannot be improved, the hard-sphere colloidal system can be regarded as a very effective model for crystallization processes. In view of the widespread applications of crystallization processes for industrial applications, further investigations may profit from a closer look at the dependence of the crystallization kinetics from the colloidal particle interaction potential.

Acknowledgements We are grateful to Sylvia Underwood, Bill van Megen and members of his group for the gift of the particles and for various stimulating discussions. In addition, we gratefully acknowledge valuable discussions with Bruce Ackerson. The present work was initiated and inspired by the late Klaus Schätzel. This work was supported financially by the Deutsche Forschunssgemeinschajt, (Scha389/6-1,2; Pa459/6-3) and the Materialwissenschaftliches Forchungszentnum, Mainz.

References

1. Pusey PN (1991) In: Hansen JP, Levesque D, Zinn-Justin J (eds) Liquids, freezing and glass transition. North Holland Amsterdam, pp 763–942
2. Pusey PN, van Megen W (1986) Nature 320:340–342
3. Hoover WG, Ree FH (1968) J Chem Phys 49:3609–3617
4. Carnahan NF, Starling KE (1969) J Chem Phys 51:635–636
5. Hall KR (1972) J Chem Phys 57:2252–2254
6. Young DA, Alder BJ (1979) J Chem Phys 70:473–481
7. Phan SE, Russel WB, Cheng Z, Zhu J, Chaikin PM, Dunsmuir JH, Ottewill RH (1996) Phys Rev E 54:6633–6645
8. Davidchack RL, Laird BB (1998) J Chem Phys 108:9452–9462
9. Antl L, Goodwin JW, Hill RD, Ottewill RH, Owens SM, Papworth S, Waters JA (1986) Colloids Surf 17:67–78
10. Philipse AP, Vrij A (1989) J Colloid Interface Sci 128:121–136
11. Pusey PN, van Megen W, Bartlett P, Ackerson BJ, Rarity JG, Underwood SM (1989) Phys Rev Lett 63:2573–2756
12. Woodcock LV (1997) Nature 385:141–143
13. Dhont JKG, Smits C, Lekkerkerker HNW (1992) J Colloid Interface Sci 152:386–401
14. (a) Schätzel K, Ackerson BJ (1992) Phys Rev Lett 68:337–340; (b) Schätzel K, Ackerson BJ (1993) Phys Rev E 48:3766–3777
15. He Y, Ackerson BJ, van Megen W, Underwood SM, Schätzel K (1993) Phys Rev E 54:5286–5297
16. Harland JL, Henderson SJ, Underwood SM, van Megen W (1995) Phys Rev Lett 75:3572–3575
17. Harland JL, van Megen W (1997) Phys Rev E 55:3054–3067
18. Russel WB (1990) Phase Transitions 21:127–137
19. Palberg T (1999) J Phys Condens Matter 11:323–360
20. Becker R, Döring W (1935) Ann Phys 24:719–752
21. Frenkel J (1946) Kinetic theory of liquids. Oxford University Press, Oxford
22. Kelton KF (1991) In: Ehrenreich H, Turnbull O (eds) Solid state physics, vol 45, Academic, New York, pp 75–177
23. Brugmans MJP, Vos WL (1995) J Chem Phys 103:2661–2669
24. van Duijneveldt (1994) Thesis. Utrecht
25. Heymann A (1997) Thesis. Kiel
26. Ohnesorge R, Löwen H, Wagner H (1994) Phys Rev E 50:4801–4809
27. Kyrlidis A, Brown RA (1995) Phys Rev E 51:5832–5845
28. Curtin WA (1989) Phys Rev B 39:6775–6791
29. Marr DW, Gast AP (1993) Phys Rev E 47:1212–1221
30. Marr DWM (1995) J Chem Phys 102:8283–8285
31. (a) Marr DW, Gast AP (1994) Langmuir 10:1348–1350; (b) Marr DW, East AP (1995) Phys Rev E 52:4058–4062
32. Aastuen DJW, Clark NA, Cotter LK, Ackerson BJ (1986) Phys Rev Lett 57:1733–1736
33. Würth M, Schwarz J, Culis F, Leiderer P, Palberg T (1995) Phys Rev E 52:6415–6423
34. He Y, Olivier B, Ackerson BJ (1997) Langmuir 13:1408–1412
35. Russel WB, Chaikin PM, Zhu J, Meyer WV, Rogers R (1997) Langmuir 13: 3871–3881
36. Tokuyama M, Oppenheim I (1995) Physica A 216:85–119
37. Heymann A, Stipp A, Sinn C, Palberg T (1998) J Colloid Interface Sci 207:119–127
38. Underwood SM, Taylor JR, van Megen W (1994) Langmuir 10:3550–3554
39. Heymann A, Sinn C, Palberg T (2000) Phys Rev E 62:813–820
40. Paulin SE, Ackerson BJ (1990) Phys Rev Lett 64:2663–2666
41. Ottewill RH, Livsey I (1987) Polymer 28:109–113
42. Ackerson BJ, Schätzel K (1995) Phys Rev E 52:6448–6460
43. (a) Furukawa H (1984) Physica A 123:497–515; (b) Furukawa (1986) Phys Rev B 33:638–640
44. Percus JK, Yevick GY (1958) Phys Rev 110:1–13
45. Heymann A, Stipp A, Schätzel K (1995) Nouvo Cimento D 16:1149–1157
46. Gránásy L, Iglói F (1997) J Chem Phys 107:3634–3644
47. Bolhuis PG, Kofke DA (1996) Phys Rev E 54:634–643
48. Bartlett P (1998) J Chem Phys 109:10970–10975
49. Henderson SI, Mortensen TC, van Megen W (1996) Physica A 233:102–116
50. Phan SE, Russel WB, Zhu J, Chaikin PM (1998) J Chem Phys 108:9789–9795